Disentangling phonon channels in nanoscale heat transport

Samik Mukherjee [1,*] Marcin Wajs,[1] Maria de la Mata,[2,†] Uri Givan,[3] Stephan Senz,[3] Jordi Arbiol [2,4]
Sebastien Francoeur [1] and Oussama Moutanabbir [1,‡]

[1]*Department of Engineering Physics, École Polytechnique de Montréal, Case Postale 6079, Succursale Centre-Ville, Montréal,*
Québec, Canada H3C 3A7
[2]*Catalan Institute of Nanoscience and Nanotechnology (ICN2), CSIC and BIST, Campus UAB,*
Bellaterra, 08193 Barcelona, Catalonia, Spain
[3]*Max Planck Institute of Microstructure Physics, Weinberg 2, Halle (Saale) 06120, Germany*
[4]*ICREA, Pg. Lluís Companys 23, 08010 Barcelona, Catalonia, Spain*

Phonon surface scattering has been at the core of heat transport engineering in nanoscale devices. Herein, we demonstrate that this phonon pathway can be the sole mechanism only below a critical, size-dependent temperature. Above this temperature, the lattice phonon scattering coexists along with surface effects. By tailoring the mass disorder at the atomic level, the lattice dynamics in nanowires was artificially controlled without affecting morphology, crystallinity, chemical composition, or electronic properties, thus allowing the mapping of the *temperature-thermal conductivity-diameter* triple parameter space. This led to the identification of the critical temperature below which the effects of lattice mass disorder are suppressed to an extent that phonon transport becomes governed entirely by the surface. This behavior is discussed based on a modified Landauer-Datta-Lundstrom near-equilibrium transport model. Besides disentangling the main phonon scattering mechanisms, the established framework also provides the necessary input to further advance the design and modeling of heat transport in semiconductor nanoscale systems.

I. INTRODUCTION

Phonon transport in a crystal is controlled by the surface as well as lattice effects [1,2]. The latter dominates in bulk materials and include defects, isotope disorder, charge carriers, and anharmonic scattering channels. Surface scattering is, however, prevalent in nanoscale materials and has been at the center of the recently expended efforts to engineer thermal transport at the nanoscale [3–9]. In this regard, semiconductor nanowires (NWs) have been extensively studied as a unique playground for phonon engineering, combining the shape anisotropy and large surface-to-volume ratio [10–16]. In NWs, the phonon-surface interaction renormalizes the phonon lifetime [3,17,18], shows evidence of Anderson localization of phonons [4,5], alters the dominant phonon wavelength in the NW [6], and tunes the NW thermal conductivity below the Casimir limit [7,8,17]. Despite the expected overwhelming dominance of surface scattering, lattice effects must also persist because of the NW finite diameter. For example, a small degree of lattice disorder in alloyed NWs can act as a low-pass filter, suppressing the high-frequency phonon modes [19], while on the other hand, a short-range spatial correlation in the mass disorder can act as a high-pass filter [20]. Thermal transport in NWs was also reported to be anisotropic, depending on the crystal orientation [21]. These studies indicate that, along with surface scattering, thermal transport in nanoscale structures underlies a subtle but important contribution from the crystalline lattice as well. However, the exact individual contributions of these mechanisms remain hitherto undiscovered and experimentally inaccessible. This work addresses this fundamental question by establishing an experimental framework to track and distinguish the inherently intertwined lattice and surface scatterings. By tailoring the lattice disorder in silicon (Si) NWs, while keeping the chemical composition, crystallinity, electronic properties, and morphology intact, the work demonstrates that the temperature-dependent effects and the size-dependent effects on phonon transport can indeed be disentangled.

II. EXPERIMENTAL DETAILS

The vapor-liquid-solid (VLS) method was employed to grow the NWs, with gold (Au) acting as the catalyst. For this, Si substrates underwent degreasing in acetone, followed by a dip in 2% hydrofluoric (HF) acid for 2 min to remove the native oxide, followed by rinsing in deionized water. Next, 2-nm-thick Au films were then deposited on the substrates before loading them into the ultrahigh vacuum chemical-vapor-deposition (UHV-CVD) chamber. Au-Si eutectic droplets were formed by annealing the substrate at 450 °C for 20 min. Mass-disorder engineering is achieved

---

*samik.mukherjee@polymtl.ca

†Present address: Departamento de Ciencia de los Materiales, Ing. Met. y Qca. Inorg., IMEYMAT, Universidad de Cádiz, 11510 Puerto Real, Spain.

‡oussama.moutanabbir@polymtl.ca

using isotopically enriched ^{28}Si H$_4$ and ^{30}Si H$_4$ precursors, with an isotopic purity higher than 99.9% [22]. The NWs discussed in this work are either isotopically pure ^{30}Si NWs or isotopically mixed ^{28}Si$_x$ ^{30}Si$_{1-x}$ ($x \sim 0.4$) NWs. The two sets of NWs are therefore chemically and morphologically identical. Additionally, the two sets of NWs are electrically identical since the isotopic mass disorder is known to have a negligible effect on the electrical properties of a material [23]. The microstructure of as-grown NWs was investigated using scanning transmission electron microscopy (STEM) in a probe-corrected FEI Titan 60-300, equipped with a high brightness field emission gun and a CETCOR corrector from CEOS.

Raman measurements were performed on individual NWs in a custom micro-Raman setup at $\lambda_{ex} = 532$ nm laser excitations. The laser was focused on the sample with a $100\times$ (NA 0.85) objective with a spatial resolution approaching the diffraction limit. The laser power density incident on the sample was measured using a hand-held power meter. The laser spot size was $\sim 1\,\mu$m. The spectra were acquired using a liquid-nitrogen cooled charged-coupled device camera (JY Symphony) mounted on a Jobin-Yvon Triax iHR550 spectrometer (grating 1800 g mm^{-1}) with a precision of 0.2 cm^{-1}. During the laser exposure, the sample was mounted inside a liquid-He cryostat that enabled adjusting the base temperature from 300 K down to 4 K, with temperature stability of 80 mK. The samples were held under a high vacuum of below 10^{-6} Torr. The spectrometer calibration was done using the Raman peak position of bulk silicon of 520.8 cm^{-1}, at 300 K. Prior to the Raman measurements, a suspension was first prepared by putting a small piece of the as-grown sample in acetone under ultrasonic vibration for 10 min. The suspension was then dispersed on two different types of substrates (see the Supplemental Material [24]): first, a Au-coated Si substrate and second a commercial Au-grid with 4-μm sized holes. The first substrate was used for investigating such intrinsic properties of the NWs, wherein any laser-induced heating effect is undesirable. The Au-coated Si substrate underneath the NWs provides good thermal contact and acts as a heat sink that can quickly dissipate any laser-induced heat. The second substrate was used for the transport studies based on power-dependent measurements. This increases the laser-induced heating effect of the NWs and suppresses any underlying effect of the substrate on the transport measurements.

III. RESULTS AND DISCUSSION

Figure 1 shows a representative high-angle dark-field STEM (HAADF-STEM) image of an isotopically mixed ^{28}Si$_{0.4}$ ^{30}Si$_{0.6}$ NW at progressively increasing magnification. The fast Fourier transform (FFT) indicates the NW growth orientation. The STEM analysis of isotopically lattice-ordered ^{30}Si NWs (not shown here) exhibits a similar microstructure. Both NW sets were found to have a mean diameter of ~ 55 nm, with 2–3 nm of native oxide at the surface. Figure 2(a) displays the Si-Si longitudinal optical (LO) phonon mode of single ^{30}Si (left) and ^{28}Si$_{0.4}$ ^{30}Si$_{0.6}$ (right) NWs, recorded at three different base temperatures. The data indicate a consistent redshift of the peak position in both sets of NWs, as the base temperature increases. Figure 2(b) summarizes
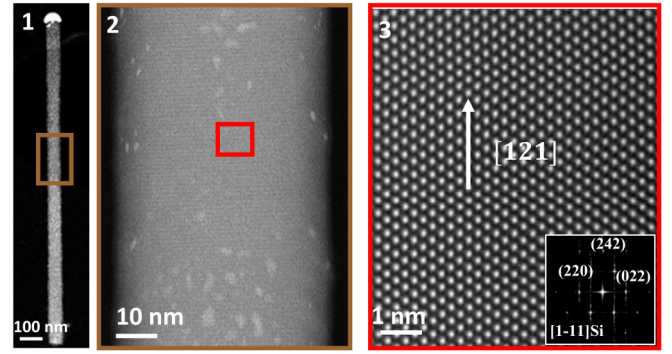
FIG. 1. HAADF image from HR-STEM analysis of a ^{28}Si$_{0.4}$ ^{30}Si$_{0.6}$ NW at different magnifications.

this evolution over the broader temperature range 4–300 K. The redshift of phonon energy from the harmonic frequency (ω_0) with increasing temperature is due to quasiharmonic effect arising from changes in crystal volume ($\Delta\omega_{vol}$) and the anharmonic phonon-phonon coupling ($\Delta\omega_{anh}$), both being temperature dependent. $\Delta\omega_{vol}(T)$ depends on the mode Gruneisen parameter, the volume thermal expansion coefficient, and can be expressed as $\Delta\omega_{vol}(T) = \omega_0\{e^{-3AT} - 1\}$ (see [24] for details related to parameter A). $\Delta\omega_{anh}(T)$ can be expressed according to the model by Klemens and Balkanski *et al.* [25,26], considering the decay of an optical phonon into two and three lower energy phonons:

$$\Delta\omega_{anh}(T) = B\left\{1 + \frac{2}{e^{\hbar\omega_0/2k_BT} - 1}\right\}$$
$$+ C\left\{1 + \frac{3}{e^{\hbar\omega_0/3k_BT} - 1} + \frac{3}{(e^{\hbar\omega_0/3k_BT} - 1)^2}\right\}, \tag{1}$$
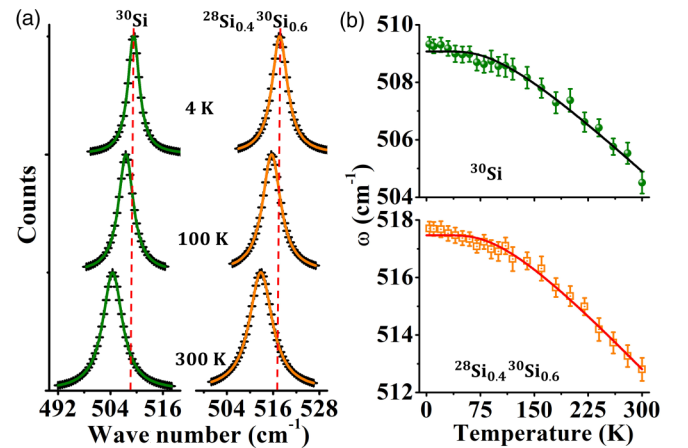
FIG. 2. (a) Back-scattering micro-Raman spectra, collected at different ambient temperatures, showing the LO phonon mode of a ^{30}Si NWs (left) and a ^{28}Si$_{0.4}$ ^{30}Si$_{0.6}$ NWs (right). The Voigt fits are shown as solid lines. The vertical red dotted line marks the peak positions of the LO modes at 4 K. (b) The evolution of Si-Si peak position (ω) as a function of ambient temperature. The fit to the ω vs T data is done using Eq. (1) (solid lines). From the fits, the parameter A in Eq. (1) was found to be 2.63×10^{-3} K^{-1} and 2.70×10^{-3} K^{-1}, while the parameter B was found to be -3.96 cm^{-1} and -3.93 cm^{-1}, for the ^{30}Si NWs and the ^{28}Si$_{0.4}$ ^{30}Si$_{0.6}$ NWs, respectively.

where B and C are cubic and quartic anharmonic coupling constants. Finally, the frequency of a phonon mode at a temperature T can be expressed as $\omega(T) = \omega_0 + \Delta\omega_{vol}(T) + \Delta\omega_{anh}(T)$. The data in Fig. 2(b) were fitted using this equation (solid lines) yielding the key fitting parameter ω_0 of $(512.3 \pm 0.3)\,cm^{-1}$ and $(521.7 \pm 0.3)\,cm^{-1}$ for ^{30}Si and $^{28}Si_{0.4}\,^{30}Si_{0.6}$ NWs, respectively. The value of C, the quartic anharmonic constant, was found from the curve fittings to be $\sim 10^{-4}\,cm^{-1}$, for both ^{30}Si NWs and $^{28}Si_{0.4}\,^{30}Si_{0.6}$ NWs. Consequently, the quartic anharmonicity can be excluded from the observed temperature-induced redshift of the LO modes for both sets of NWs. The total redshift in ω from 4 to 300 K is insensitive to the isotopic content since neither of the two effects depends on the lattice-disorder [27].

Next, the evolution of LO mode peak position was measured as a function of the incident laser power (LP), at fixed ambient temperatures. Examples of this evolution as a function of LP at 140 K are displayed in Figs. 3(a) and 3(b), for ^{30}Si NWs and $^{28}Si_{0.4}\,^{30}Si_{0.6}$ NWs, respectively. The peak position typically undergoes a redshift with increasing LP, indicative of laser-induced local heating [28,29], and subsequent increase in the local temperature of the NWs (T_{NW}^{rise}). At a first glance, it is clear that for the same change in the LP, the total redshift in peak position of $^{28}Si_{0.4}\,^{30}Si_{0.6}$ NWs [Fig. 3(b)] is larger than that of ^{30}Si NWs [Fig. 3(a)]. This means that the isotopically disordered NWs are heating up much *easier* than the isotopically pure ones. This effect is best summed up by extracting T_{NW}^{rise} of the two sets of NWs, as a function of LP. The base temperature (T) in the expression of $\omega(T)$ was replaced by T_{NW}^{rise}, where T_{NW}^{rise} is the sum of the base temperature (T) and the increase in the NW local temperature due to laser-induced heating. The exponentials in the expression of $\omega(T)$ were also expanded into a Maclaurin series and terminated at the linear term. Combining all these factors, T_{NW}^{rise} is obtained as

$$T_{NW}^{rise} = \frac{(\omega_0 + B) - \omega(T_{NW}^{rise})}{\left[3A\omega_0 - \frac{4k_B B}{\hbar\omega_0}\right]}. \tag{2}$$

Note that the parameters ω_0, A, and B in the right-hand side of Eq. (2) are known for both NW types. The evolution of T_{NW}^{rise} as a function of the LP for ^{30}Si NWs and $^{28}Si_{0.4}\,^{30}Si_{0.6}$ NWs is also displayed in Figs. 3(a) and 3(b), respectively. The rate of change in T_{NW}^{rise} with the incident LP is inversely related to κ_T (thermal conductivity) [22,30]. The higher the κ_T, the easier it is for the laser-induced heat to flow away and the *slower* is the rate of increase in T_{NW}^{rise} with incident LP. Note that only the linear regime of the T_{NW}^{rise} vs LP graph has been used in the subsequent analysis. Figure 3(c) compares this regime for ^{30}Si NWs and $^{28}Si_{0.4}\,^{30}Si_{0.6}$ NWs at 140 K (top) and 60 K (bottom). At 140 K, the ratio of the respective slopes shows that T_{NW}^{rise} of $^{28}Si_{0.4}\,^{30}Si_{0.6}$ NWs increases $\sim 1.30\times$ *faster* with LP than that of ^{30}Si NWs. This indicates that κ_T of $^{28}Si_{0.4}\,^{30}Si_{0.6}$ NWs is $\sim 30\%$ lower than that of ^{30}Si NWs at 140 K. This reduction stems from the isotope scattering in lattice-disordered NWs. The slope ratio reaches unity at 60 K, which indicates identical κ_T for both isotopically mixed and isotopically pure NWs. This means that the effect of isotope-induced mass disorder has been suppressed at 60 K, leaving surface scattering as the dominant mecha-
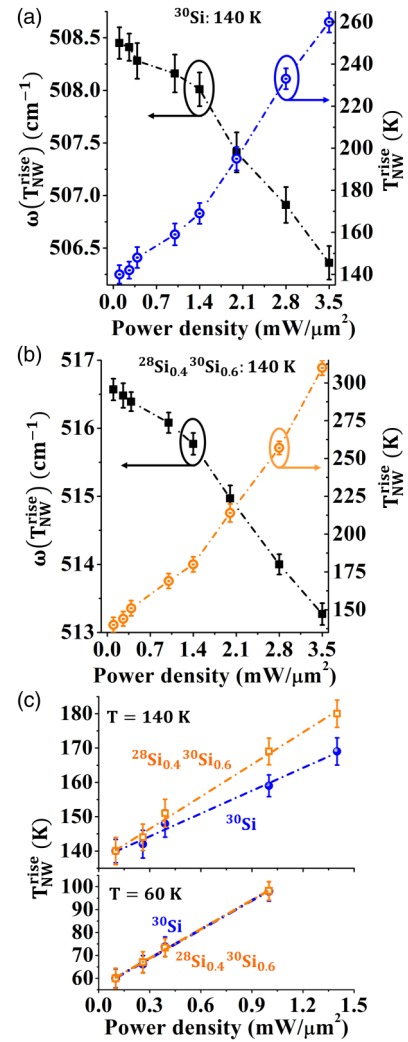
FIG. 3. Evolution of $\omega(T_{NW}^{rise})$ and T_{NW}^{rise} of (a) ^{30}Si NWs and (b) $^{28}Si_{0.4}\,^{30}Si_{0.6}$ NWs, as a function of laser power at 140 K. The data are averaged over 10–15 individual NWs. The corresponding error bars in $\omega(T_{NW}^{rise})$ are the standard deviation of the data. The error bars associated with the T_{NW}^{rise} comes from two sources: the standard deviation (error bars) associated with the mean value of $\omega(T_{NW}^{rise})$ and the uncertainty associated with the value of ω_0 estimated from the fit. (c) Evolution in the linear regime of T_{NW}^{rise} as a function of the laser power of ^{30}Si NWs and the $^{28}Si_{0.4}\,^{30}Si_{0.6}$ NWs, at 140 K (top) and 60 K (bottom). The dot-dash-dot lines are the linear fit to the corresponding data.

nism determining the overall phonon lifetime. Also, note the difference in the slope of T_{NW}^{rise} at 140 K and that at 60 K. For example, for ^{30}Si NWs at 60 K, the slope is $\sim 1.45\times$ larger than that at 140 K, indicating that κ_T of ^{30}Si NWs at 60 K is reduced by $\sim 45\%$ relative to its value at 140 K. The temperature evolution of κ_T of both the NW sets is discussed next.

Figure 4(a) exhibits the evolution of κ_T with temperature, where κ_T is always given relative to that of ^{30}Si NWs at 300 K. The temperature evolution of κ_T is quite different from bulk materials. The isotope effect on κ_T of bulk semiconductors becomes most prominent at a material-specific temperature [31–33], where κ_T reaches the maximum between
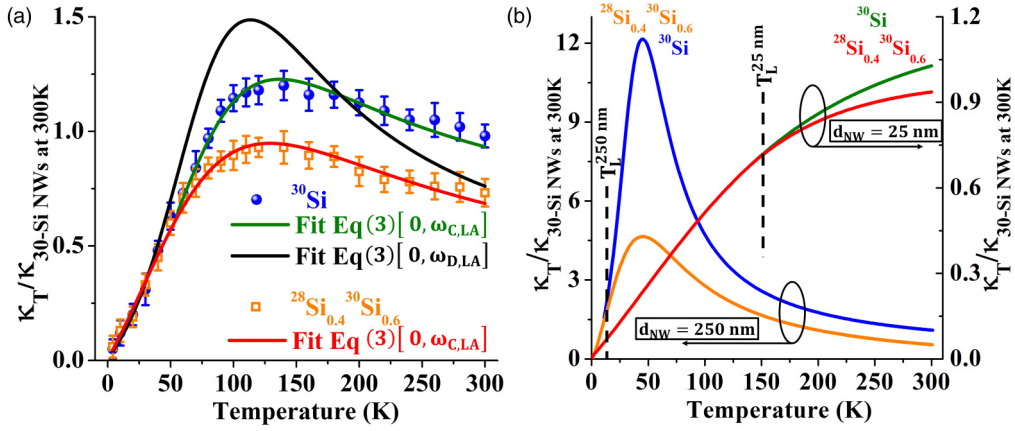
FIG. 4. (a) Evolution of κ_T of ^{30}Si NWs and ^{28}Si$_{0.4}$ ^{30}Si$_{0.6}$ NWs as a function of the ambient temperature. The data are normalized to κ_T of ^{30}Si NWs at 300 K. The solid-colored lines are fit to the data using Eq. (3) (see text for details). (b) Simulated κ_T of ^{30}Si NWs and ^{28}Si$_{0.4}$ ^{30}Si$_{0.6}$ NWs, as a function of ambient temperature, at diameter extremities of 250 and 25 nm. In order to be consistent with the experimental data in (a), the simulated data in (b) were also normalized to κ_T of ^{30}Si NWs at 300 K.

the low-temperature surface effects and the high-temperature anharmonic effects dominated regions. In NWs, however, phonon surface scattering competes with all other scattering mechanisms, even at elevated temperatures [34–36]. In the following, the subtleties of this behavior are further discussed. First, we start by examining the Landauer-Datta-Lundstrom (LDL) transport model [37,38], which defines the lattice thermal conductance (K_T) under near-equilibrium conditions as [38,39]

$$K_T = \sum_{j=LA,TA} \frac{k_B^2 T}{h} \int_j M_j^{ph}(\omega) W^{ph}(\omega, T) \mathcal{T}_j^{ph}(\omega, T) d\omega, \quad (3)$$

where the summation runs over the longitudinal acoustic (LA) and the doubly degenerate transverse acoustic (TA) phonon modes. Background information related to the LDL model that highlights the physics underlying Eq. (3) can be found in [24]. $M_j^{ph}(\omega)$ is the total number of channels available to the mode "j" for heat conduction and is given by the cross section of the heat conductor times the phonon velocity times the density of states, $D_j^{ph}(\omega) = \omega^2/2\pi^2 v_j^3$ [40]. $W^{ph}(\omega, T)$ is the window function that selects only those channels, out of all the available channels, which take part in thermal conduction. $W^{ph}(\omega, T) = (\hbar\omega/k_B T)^2(-\partial n_{Bose}/\partial \omega)$, where $n_{Bose} = [e^{\hbar\omega/k_B T} - 1]^{-1}$ is the equilibrium Bose-Einstein factor. $\mathcal{T}_j^{ph}(\omega, T)$ is the transmission function that defines the probability that the jth mode is transmitted along the length (L) of the heat conductor, without backscattering. $\mathcal{T}_j^{ph}(\omega, T) \approx f v_j \tau_j(\omega, T)/L$, where v_j is the mode velocity and $\tau_j(\omega, T)$ is the mode lifetime. f is a prefactor which accounts for the backscattering mean-free path [41].

The following scattering mechanisms were considered to calculate the phonon lifetime [24]: the normal and Umklapp anharmonic scattering, scattering from mass disorder, and surface scattering of phonons [32,35,42–44]. Additionally, the decay of high-energy optical phonons into acoustic phonons was also considered (see the phonon dispersion relation in Si in Refs. [45,46]), which was shown to act as a gener-

ation rate of acoustic phonons, partially counteracting their scattering rate at the same energy [47,48]. Finally, the total acoustic phonon scattering rate was calculated according to the Matthiessen rule, after neglecting any phonon confinement effects. The experimental data in Fig. 4(a) was fitted using Eq. (3), with the specularity factor (P) and the constants $C_{LA(TA)}^{M(P)}$ [24] as free parameters. The upper limit of the integral in Eq. (3) was initially set at Debye frequencies [$\omega_{D,LA(TA)} = k_B \theta_{D,LA(TA)}/\hbar$] in Si: 76.7 THz for the LA mode and 31.4 THz for the TA mode.

The analysis was first carried out on the data for ^{30}Si NWs in Fig. 4(a). Clearly, the LDL model (solid black line) disagrees with the experimental data, and more so above 50 K. The reasons for this discrepancy lie in the bulklike Debye phonon spectrum, which might overestimate the contribution of the phonon Umklapp scattering rate [44] and that of $M_j^{ph}(\omega)$ [41] in Eq. (3). The optimization was done by choosing a lower cutoff frequency on a trial-and-error basis [44]. The solid green line in Fig. 4(a) was obtained after the optimization, yielding a cutoff frequency ($\omega_{C, LA}$) of 51.7 THz for the LA mode. The optimization also found that lowering the cutoff frequency of the TA mode impacts the quality of the fit only nominally and was, therefore, maintained at its Debye frequency to avoid an additional undetermined parameter in the model. The values of P and $C_{LA(TA)}^P$ for ^{30}Si NWs were found to be 0.26 and 14.86 × 10^4 s^2 (22.01 × 10^6 s^4), respectively (see the validation of this approach in [24]). The value of P was taken the same for the two sets of NWs as they were grown under identical conditions, while only $C_{LA(TA)}^M$ was kept as a free parameter. The obtained result is displayed by the solid red line in Fig. 4(a), with $C_{LA(TA)}^M = 17.34 × 10^4$ s^2 (20.21 × 10^6 s^4). The modified LDL model, with all its optimized parameters, was then used to simulate the evolution of κ_T with temperature, for both ^{30}Si NWs and ^{28}Si$_{0.4}$ ^{30}Si$_{0.6}$ NWs, by varying the diameter (d_{NW}) from 25 nm up to 250 nm. The results are shown in Fig. 4(b) at the two extreme ends of the diameter range. Simulations of κ_T vs T at a few intermediate values of d_{NW} are shown in [24]. The temperature behavior of κ_T in Fig. 4(b) is remarkably sensitive
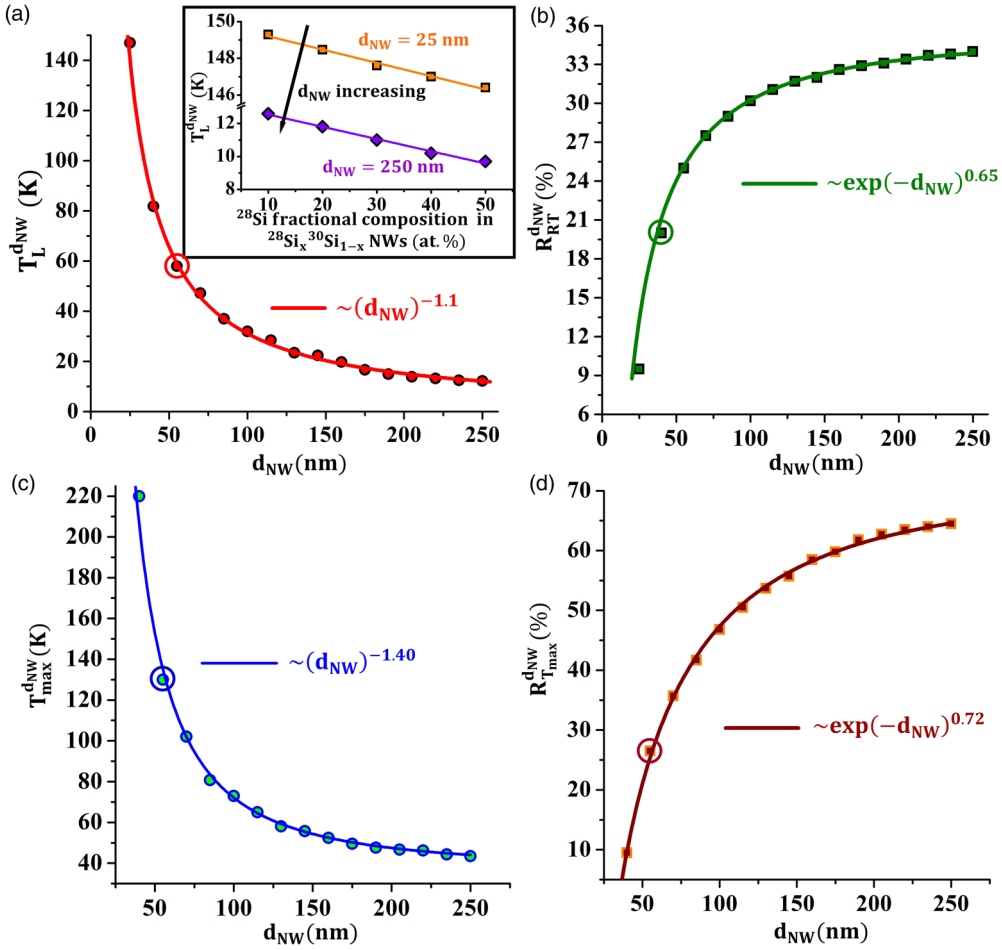
FIG. 5. (a) Evolution of $T_L^{d_{NW}}$ as a function of the NW diameter (d_{NW}). The solid red line is a power-law fit to the simulated data. Inset: Evolution of $T_L^{d_{NW}}$ as a function of the fractional composition of ^{28}Si isotope within a ^{28}Si$_{0.4}$ ^{30}Si$_{0.6}$ NW, at diameter extremities of 25 and 250 nm. The solid lines are linear fit to the respective data. (b) The evolution $R_{RT}^{d_{NW}}$ as a function of d_{NW}. The solid green line is an exponential fit to the simulated data, showing a $\sim\exp(-d_{NW})^{0.65}$ dependence on d_{NW}. (c) The evolution of $T_{max}^{d_{NW}}$ as a function of d_{NW}. The solid blue line is the fit to the simulated data, showing a $\sim(d_{NW})^{-1.4}$ dependence. (d) The evolution of $R_{T_{max}}^{d_{NW}}$ as a function of d_{NW}. The solid brown line is the fit to the simulated data, showing a $\sim\exp(-d_{NW})^{0.72}$ dependence. Note that the NWs with d_{NW} of 25 nm never reache T_{max} within the temperature range of 300 K considered in this work [see Fig. 4(b)]. Consequently, the data in (c) and (d) start at $d_{NW} = 40$ nm and do not show the data point corresponding to $d_{NW} = 25$ nm. In (a)–(d), the simulated data point corresponding to $d_{NW} = 55$ nm (the average diameter of the NWs investigated experimentally in this work) is highlighted using the colored circles.

to d_{NW}, which highlights the varying contribution of surface scattering to the phonon lifetime in the NWs.

From the analysis above, it becomes possible to track the temperature limit of mass disorder-induced phonon scattering ($T_L^{d_{NW}}$), which is the temperature at which any effect of the lattice on κ_T vanishes leaving the phonon surface scattering as the sole mechanism (see the black dotted line in Fig. 4(b), denoting T_L^{250nm} and T_L^{25nm}). Figure 5(a) shows the evolution of $T_L^{d_{NW}}$ as a function of d_{NW}. The dependence on d_{NW} is very close to being hyperbolic, as extracted from the power-law fit. Given that $T_L^{d_{NW}}$ is the temperature below which lattice mass-disorder effect on κ_T is suppressed, its evolution as a function of the mass variance was also investigated. $T_L^{d_{NW}}$ was found to exhibit a linear behavior [inset of Fig. 5(a)], decreasing by ~ 0.85 K for every 10.0 at. % increment in the ^{28}Si concentration [49]. Interestingly, the influence of the mass variance on $T_L^{d_{NW}}$ does not show any clear sensitivity to d_{NW}, as reflected by the same slope of the NWs at the diameter extremities of

25 nm and 250 nm. Our analysis also allowed to investigate and quantify the behavior of other key parameters: Fig. 5(b) shows the reduction in room temperature κ_T due to mass-disorder ($R_{RT}^{d_{NW}}$); Fig. 5(c) shows the temperature at which κ_T reaches its maximum value ($T_{max}^{d_{NW}}$); and Fig. 5(d) shows the reduction in κ_{max} at $T_{max}^{d_{NW}}$ due to mass-disorder ($R_{T_{max}}^{d_{NW}}$). $T_{max}^{d_{NW}}$ was found to have a $\sim(d_{NW})^{-1.4}$ dependence, while $R_{RT}^{d_{NW}}$ and $R_{T_{max}}^{d_{NW}}$ were found to depend on d_{NW} as $\sim\exp(-d_{NW})^{0.65}$ and $\sim\exp(-d_{NW})^{0.72}$, respectively.

IV. CONCLUSION

To conclude, by artificially controlling the mass-disorder and lattice dynamics in NWs, the analyses above provide a framework to evaluate the *temperature-κ_T-diameter* triple-parameter space. The obtained results demonstrate that nanoscale phonon transport is indeed not all about the surface,

but rather there exists a size-dependent temperature regime where the lattice also contributed to the heat transport. The work also identifies the boundary between this regime and the purely surface-dominated phonon transport regime and elucidates how this boundary evolves as a function of the diameter and the extent of mass disorder in the crystalline lattice. By unraveling these fundamental aspects, this work disentangles the primary phonon scattering channels that strongly influence the thermal transport. This knowledge is crucial to guide the design and modeling of future nanoscale phononic and thermoelectric devices and heat management platforms.

[1] D. G. Cahill, W. K. Ford, K. E. Goodson, G. D. Mahan, A. Majumdar, H. J. Maris, R. Merlin, and S. R. Phillpot, Nanoscale thermal transport, J. Appl. Phys. **93**, 793 (2003).

[2] D. G. Cahill, P. V. Braun, G. Chen, D. R. Clarke, S. Fan, K. E. Goodson, P. Keblinski, W. P. King, G. D. Mahan, A. Majumdar, H. J. Maris, S. R. Phillpot, E. Pop, and L. Shi, Nanoscale thermal transport. II. 2003–2012, Appl. Phys. Rev. **1**, 011305 (2014).

[3] A. L. Moore, S. K. Saha, R. S. Prasher, and L. Shi, Phonon backscattering and thermal conductivity suppression in sawtooth nanowires, Appl. Phys. Lett. **93**, 083112 (2008).

[4] P. Markoš and K. A. Muttalib, Phonon localization in nanowires dominated by surface roughness, Phys. Rev. B **99**, 134208 (2019).

[5] S. Xiong, K. Sääskilahti, Y. A. Kosevich, H. Han, D. Donadio, and S. Volz, Blocking Phonon Transport by Structural Resonances in Alloy-Based Nanophononic Metamaterials Leads to Ultralow Thermal Conductivity, Phys. Rev. Lett. **117**, 025503 (2016).

[6] A. Malhotra and M. Maldovan, Impact of phonon surface scattering on thermal energy distribution of Si and SiGe Nanowires, Sci. Rep. **6**, 25818 (2016).

[7] J. Lim, K. Hippalgaonkar, S. C. Andrews, A. Majumdar, and P. Yang, Quantifying surface roughness effects on phonon transport in silicon nanowires, Nano Lett. **12**, 2475 (2012).

[8] J. Sadhu and S. Sinha, Room-temperature phonon boundary scattering below the casimir limit, Phys. Rev. B **84**, 115450 (2011).

[9] G. Zhang and B. Li, Impacts of doping on thermal and thermoelectric properties of nanomaterials, Nanoscale **2**, 1058 (2010).

[10] C.-Y. Wen, J. Tersoff, K. Hillerich, M. C. Reuter, J. H. Park, S. Kodambaka, E. A. Stach, and F. M. Ross, Periodically Changing Morphology of the Growth Interface in Si, Ge, and GaP Nanowires, Phys. Rev. Lett. **107**, 025503 (2011).

[11] H. Kim, Y. H. Park, I. Kim, J. Kim, H. J. Choi, and W. Kim, Effect of surface roughness on thermal conductivity of VLS-grown rough Si1-xGex nanowires, Appl. Phys. A: Mater. Sci. Process. **104**, 23 (2011).

[12] A. I. Hochbaum, R. Chen, R. D. Delgado, W. Liang, E. C. Garnett, M. Najarian, A. Majumdar, and P. Yang, Enhanced thermoelectric performance of rough silicon nanowires, Nature (London) **451**, 163 (2008).

[13] T. K. Hsiao, H. K. Chang, S. C. Liou, M. W. Chu, S. C. Lee, and C. W. Chang, Observation of room erature ballistic thermal conduction persisting over 8.3 μm in SiGe nanowires, Nat. Nanotechnol. **8**, 534 (2013).

[14] D. Vakulov, S. Gireesan, M. Y. Swinkels, R. Chavez, T. Vogelaar, P. Torres, A. Campo, M. De Luca, M. A. Verheijen, S. Koelling, L. Gagliano, J. E. M. Haverkort, F. X. Alvarez, P. A. Bobbert, I. Zardo, and E. P. A. M. Bakkers, Ballistic phonons in ultrathin nanowires, Nano Lett. **20**, 2703 (2020).

[15] M. Y. Swinkels, M. R. van Delft, D. S. Oliveira, A. Cavalli, I. Zardo, R. W. van der Heijden, and E. P. A. M. Bakkers, Diameter dependence of the thermal conductivity of InAs nanowires, Nanotechnology **26**, 385401 (2015).

[16] B. Hamdou, J. Gooth, A. Dorn, E. Pippel, and K. Nielsch, Surface state dominated transport in topological insulator Bi2Te3 nanowires, Appl. Phys. Lett. **103**, 193107 (2013).

[17] P. Martin, Z. Aksamija, E. Pop, and U. Ravaioli, Impact of Phonon-Surface Roughness Scattering on Thermal Conductivity of Thin Si Nanowires, Phys. Rev. Lett. **102**, 125503 (2009).

[18] P. N. Martin, Z. Aksamija, E. Pop, and U. Ravaioli, Prediction of reduced thermal conductivity in nano-engineered rough semiconductor nanowires, J. Phys. Conf. Ser. **193**, 012010 (2009).

[19] G. Xie, Y. Guo, X. Wei, K. Zhang, L. Sun, J. Zhong, G. Zhang, and Y. W. Zhang, Phonon mean free path spectrum and thermal conductivity for Si1-xGex nanowires, Appl. Phys. Lett. **104**, 233901 (2014).

[20] Z. Y. Ong and G. Zhang, Enhancement and reduction of one-dimensional heat conduction with correlated mass disorder, Phys. Rev. B **90**, 155459 (2014).

[21] T. Markussen, A.-P. Jauho, and M. Brandbyge, Heat conductance is strongly anisotropic for pristine silicon nanowires, Nano Lett. **8**, 3771 (2008).

[22] S. Mukherjee, U. Givan, S. Senz, A. Bergeron, S. Francoeur, M. de la Mata, J. Arbiol, T. Sekiguchi, K. M. Itoh, D. Isheim, D. N. Seidman, and O. Moutanabbir, Phonon engineering in

isotopically disordered silicon nanowires, Nano Lett. **15**, 3885 (2015).

[23] A. P. Zhernov and A. V. Inyushkin, Kinetic coefficients in isotopically disordered crystals, Phys. Usp. **45**, 527 (2002).

[24] See Supplemental Material at http://link.aps.org/supplemental/10.1103/PhysRevB.104.075429 for additional details on the experimental methods, background information on the LDL model and Eqs. (1) and (3) of the main text, mathematical expressions of different phonon scattering mechanisms considered in this work, as well as additional data that were not presented in the main paper.

[25] P. G. Klemens, Anharmonic decay of optical phonons, Phys. Rev. **148**, 845 (1966).

[26] M. Balkanski, R. F. Wallis, and E. Haro, Anharmonic effects in light scattering due to optical phonons in silicon, Phys. Rev. B **28**, 1928 (1983).

[27] J. Menéndez and M. Cardona, Temperature dependence of the first-order raman scattering by phonons in Si, Ge, and α − Sn: anharmonic effects, Phys. Rev. B **29**, 2051 (1984).

[28] M. Soini, I. Zardo, E. Uccelli, S. Funk, G. Koblmüller, A. Fontcuberta i Morral, and G. Abstreiter, Thermal conductivity of GaAs nanowires studied by micro-raman spectroscopy combined with laser heating, Appl. Phys. Lett. **97**, 263107 (2010).

[29] H. Scheel, S. Khachadorian, M. Cantoro, A. Colli, A. C. Ferrari, and C. Thomsen, Silicon nanowire optical raman line shapes at cryogenic and elevated temperatures, Phys. Status Solidi **245**, 2090 (2008).

[30] S. Mukherjee, U. Givan, S. Senz, M. De La Mata, J. Arbiol, and O. Moutanabbir, Reduction of thermal conductivity in nanowires by combined engineering of crystal phase and isotope disorder, Nano Lett. **18**, 3066 (2018).

[31] R. K. Kremer, K. Graf, M. Cardona, G. G. Devyatykh, A. V. Gusev, A. M. Gibin, A. V. Inyushkin, A. N. Taldenkov, and H.-J. Pohl, Thermal conductivity of isotopically enriched 28Si: Revisited, Solid State Commun. **131**, 499 (2004).

[32] M. Asen-Palmer, K. Bartkowski, E. Gmelin, M. Cardona, A. P. Zhernov, A. V. Inyushkin, A. Taldenkov, V. I. Ozhogin, K. M. Itoh, and E. E. Haller, Thermal conductivity of germanium crystals with different isotopic compositions, Phys. Rev. B **56**, 9431 (1997).

[33] D. G. Onn, A. Witek, Y. Z. Qiu, T. R. Anthony, and W. F. Banholzer, Some Aspects of the Thermal Conductivity of Isotopically Enriched Diamond Single Crystals, Phys. Rev. Lett. **68**, 2806 (1992).

[34] D. Li, Y. Wu, P. Kim, L. Shi, P. Yang, and A. Majumdar, Thermal conductivity of individual silicon nanowires, Appl. Phys. Lett. **83**, 2934 (2003).

[35] N. Mingo, L. Yang, D. Li, and A. Majumdar, Predicting the thermal conductivity of si and ge nanowires, Nano Lett. **3**, 1713 (2003).

[36] E. K. Lee, L. Yin, Y. Lee, J. W. Lee, S. J. Lee, J. Lee, S. N. Cha, D. Whang, G. S. Hwang, K. Hippalgaonkar, A. Majumdar, C. Yu, B. L. Choi, J. M. Kim, and K. Kim, Large thermoelectric figure-of-merits from sige nanowires by simultaneously measuring electrical and thermal transport properties, Nano Lett. **12**, 2918 (2012).

[37] S. Datta, *Lessons from Nanoelectronics: A New Perspective on Transport* (World Scientific, Singapore, 2012).

[38] M. Lundstrom and C. Jeong, *Near-Equilibrium Transport: Fundamentals and Applications* (World Scientific, Singapore, 2013).

[39] Y. Kruglyak and M. Strikha, Heat flow by phonons in Landauer-Datta-Lundstrom transport model for micro- and nanoelectronics, *IEEE 35th International Conference on Electronics and Nanotechnology (ELNANO), Kyiv* 2015, p. 75-80.

[40] C. Kittel, *Introduction to Solid State Physics* (Wiley, New York, 2005).

[41] C. Jeong, S. Datta, and M. Lundstrom, Full dispersion versus debye model evaluation of lattice thermal conductivity with a landauer approach, J. Appl. Phys. **109**, 073718 (2011).

[42] D. T. Morelli, J. P. Heremans, and G. A. Slack, Estimation of the isotope effect on the lattice thermal conductivity of Group IV and Group III-V semiconductors, Phys. Rev. B **66**, 195304 (2002).

[43] P. G. Klemens, The Scattering of Low-Frequency Lattice Waves by Static Imperfections, Proc. Phys. Soc., London, Sect. A **68**, 1113 (1955).

[44] N. Mingo, Calculation of Si nanowire thermal conductivity using complete phonon dispersion relations, Phys. Rev. B **68**, 113308 (2003).

[45] S. Wei and M. Y. Chou, Ab Initio Calculation of Force Constants and Full Phonon Dispersions, Phys. Rev. Lett. **69**, 2799 (1992).

[46] S. Wei and M. Y. Chou, Phonon dispersions of silicon and germanium from first-principles calculations, Phys. Rev. B **50**, 2221 (1994).

[47] M. Kazan, S. Pereira, M. R. Correia, and P. Masri, Contribution of the decay of optical phonons into acoustic phonons to the thermal conductivity of AlN, Phys. Rev. B **77**, 180302(R) (2008).

[48] M. Kazan, G. Guisbiers, S. Pereira, M. R. Correia, P. Masri, A. Bruyant, S. Volz, and P. Royer, Thermal conductivity of silicon bulk and nanowires: effects of isotopic composition, phonon confinement, and surface roughness, J. Appl. Phys. **107**, 083503 (2010).

[49] Note that the fractional composition is indicative of the mass variance. The rate of decrease in TLdNW is only true up to ^{28}Si composition of 50.0 at. %. At this concentration, the isotopically mixed NWs attain their maximum mass variance. The lattice would start to become more ordered with a further increase in ^{28}Si concentration.